Lawrence Berkeley National Laboratory
LBL Publications

Title
A layered nonstoichiometric lepidocrocite-type sodium titanate anode material for sodium-ion batteries

Permalink
https://escholarship.org/uc/item/51n302h2

Journal
MRS Energy & Sustainability, 8(2)

ISSN
2329-2229

Authors
Yin, Wei
Alvarado, Judith
Barim, Gözde
et al.

Publication Date
2021-09-01

DOI
10.1557/s43581-021-00008-6

Peer reviewed

A Layered Nonstoichiometric Lepidocrocite-type Sodium Titanate Anode Material for Sodium-Ion Batteries

Wei Yin,[a] Judith Alvarado,[a] Gözde Barim,[a] M. C. Scott,[b,c] Xinxing Peng,[b,c] and Marca M. Doeff[a,*]

[a]*Energy Storage & Distributed Resources Division, Lawrence Berkeley National Laboratory, Berkeley, CA 94720, USA.*

[b]*Materials Science and Engineering Department, University of California at Berkeley, Berkeley CA 94720, USA*

[c]*National Center for Electron Microscopy, Molecular Foundry, Lawrence Berkeley National Laboratory, Berkeley, CA 94720, USA*

E-mail: mmdoeff@lbl.gov

Highlights

Further performance improvements of sodium-ion batteries require better-performing electrode materials, particularly anodes. The layered lepidocrocite-type sodium titanate ($Na_{0.74}Ti_{1.815}\square_{0.185}O_4 \cdot 1.27H_2O$), showing a high Na^+ storage capacity of 229 mAh g^{-1} at relatively low average voltage of ca. 0.6 V *vs*. Na^+/Na, is a promising candidate anode material.

Abstract

A lepidocrocite-structured sodium titanate prepared by ion-exchange of a Cs-containing precursor shows promise as an anode material for sodium ion batteries, with a discharge capacity of up to 229 mAh g^{-1} at an average potential of about 0.6 V *vs*. Na^+/Na. Titanium vacancies in the metal oxide layers provide additional sites for sodium intercalation in addition to interlayer sites, which accounts for the higher capacity compared to other previously reported lepidocrocite-structured titanates. By screening a series of electrolyte formulations and binders, we were able to improve the first-cycle coulombic efficiency to 81.8 % and 94.7 % respectively using CMC/SBR-based and binder-free electrodes in ether electrolytes. The electrochemical consequences of short-term air-exposure on the electrodes are also discussed.

Key words: Energy Storage, Sustainability, Ti, Intercalation

Discussion

Of all the 'beyond lithium-ion' battery systems, sodium-ion batteries are the most highly developed, with some commercialized systems ($Na_3V_2(PO_4)_2F_3$ (NVPF) / Hard Carbon)

outperforming the LiFePO$_4$/graphite lithium-ion system on many metrics including energy density. Further performance improvements (i.e., power density, energy density, lifetime) of sodium-ion batteries, however, require better-performing electrode materials. Compared to the wide variety of high-performance cathode materials (layered, polyanion, or Prussian blue analogues), the number of suitable anode materials for sodium-ion batteries is somewhat limited. Hard carbons, which have reasonably high capacity and good cycling behavior are the most widely used. However, the extremely low potentials at which sodium inserts into hard carbons raise some safety concerns. The relatively low density of hard carbon also imposes an energy density penalty. Identifying suitable alternative Na$^+$ insertion anodes remain a great challenge for the development of sodiumion batteries. Here we report on a promising stepped layered titanate anode with high capacity and moderately low average potentials vs. Na$^+$/Na and discuss its physical and electrochemical characteristics.

Introduction

Sodium-ion batteries represent a promising alternative to lithium-ion batteries, particularly for large-scale energy storage applications, where cost and resource limitations are primary concerns. With their ongoing development, state-of-art electrode materials available for sodium-ion batteries have the potential of offering comparable material-level specific energies to some lithium-ion systems.[1, 2] Compared to the wide variety of high-performance positive electrode materials (layered, polyanion, or Prussian blue analogues),[3] the number of suitable negative electrode materials for sodium-ion batteries is somewhat limited. Among the available choices, hard carbon electrodes, which have reasonably high capacity and good cycling behavior are preferred over conversion- or alloying electrodes, which usually suffer from huge volume expansion, large hysteresis, and poor reversibility.[1, 4] However, there are some safety concerns due to the extremely low potentials at which sodium inserts into hard carbon, close to the sodium plating potential. The relatively low density of hard carbon also imposes an energy density penalty.[5] To ensure the safe operation of sodium-ion batteries, it is essential to develop alternative anode materials with suitable characteristics. Towards that end, titanium-based oxides are particularly attractive candidates with average intercalation potentials ranging from 0.3 to 1.0 V vs. Na$^+$/Na (Table 1). The added advantages of titanium-based electrodes are low cost, high availability, low toxicity, potentially longer cycle life due to minimal volumetric changes upon cycling, and structural/compositional diversity which offer an opportunity to tailor their electrochemical properties depending on the target usage.

In the family of titanium-based anode materials, TiO$_2$ and its derivatives have been studied the most.[2, 6] With proper nanosizing and/or chemical modifications to ensure electronic conductivity, carbon-coated TiO$_2$ electrodes can retain 200 mAh g^{-1} in the 300th cycle when cycled at current rate of 1 C.[7] However, the achievable energy density is compromised by the relatively high storage voltage (0.8 V vs. Na$^+$/Na). Sodium titanates are another promising family of anode materials.[8] Depending on structure (layered or tunnel), a considerable amount of Na$^+$ can be reversibly stored (e.g., 200 mAh g^{-1} for sodium nonatitanate)[9] at low potentials (in the range of 0.3

2

~ 0.6 V *vs*. Na$^+$/Na).[5, 10, 11] We recently reported on several candidate sodium titanate anodes[5, 9, 11, 12] with lepidocrocite-type structures. These materials have the general formula Na$_x$Ti$_{2-y}$M$_y$O$_4$ (where M represents a variety of substituents such as Li$^+$ or Mg^{2+}). These titanates consist of two-dimensional corrugated layers formed by edge and corner shared TiO$_6$ octahedra with alkali metal ions located in-between the layers. Different lattice symmetries are possible for lepidocrocite titanates depending on the identities and positions of the interlayer species and details of the synthesis: e.g., upon heat treatment, the P-type (primitive lattice) Na$_x$Ti$_{2-x/3}$Li$_{x/3}$O$_4 \bullet n$H$_2$O ($x = 0.8$ or 0.9) transforms into the anhydrous C-type (C-based centered lattice) phase.[11, 13] Reasonably high reversible capacities are obtained for some of these materials although less than expected based on structural considerations; e.g., 140 mAh g^{-1} for P-type Na$_{0.8}$Ti$_{1.73}$Li$_{0.27}$O$_4 \bullet n$H$_2$O,[11] and 120 mAh g^{-1} for C-type Na$_{0.9}$Ti$_{1.7}$Li$_{0.3}$O$_4$.[13] A computational study indicated that both interlayer site limitations and electrostatic considerations govern the capacity that can be obtained practically, particularly for C-type structures.[12] The presence of a mobile cation such as Li in the metal oxide layer provides an additional diffusional pathway for sodium and also improves practical capacities at a given rate; Mg-substituted titanates, in contrast, perform very poorly. This observation motivated us to look for phases with vacancies in the metal oxide layers, on the assumption that these vacancies will have similar beneficial effects as mobile cations.

We selected a nonstoichiometric sodium titanate containing titanium vacancies, which can be simply prepared by exchanging Cs$^+$ for Na$^+$ in the cesium titanate Cs$_{0.74}$Ti$_{1.815}\square_{0.185}$O$_4$ and studied the electrochemical properties. The material was also assessed with different electrolyte/electrode combinations in an effort to minimize the first cycle coulombic inefficiencies.

Experimental section

Syntheses

The precursor cesium titanate Cs$_{0.74}$Ti$_{1.815}\square_{0.185}$O$_4$ was prepared by calcining under air a stoichiometric mixture of TiO$_2$ (99.8%, Sigma Aldrich) and Cs$_2$CO$_3$ (99.9%, Sigma-Aldrich) at 800 °C for 20 hours.[14] The as-prepared Cs$_{0.74}$Ti$_{1.815}\square_{0.185}$O$_4$ was then converted to the sodium form by an ion-exchange step. One gram of Cs$_{0.74}$Ti$_{1.815}\square_{0.185}$O$_4$ was stirred in 100 mL aqueous 4 M NaCl solution at 80 °C in a heated mineral oil bath for 7 days. The resulting powder was then vacuum filtered, washed, and dried at 60 °C in an incubator.

Characterization

High resolution X-ray diffraction (XRD) data was collected through the mail-in service at the 11-BM beamline at the Advanced Photon Source (APS) of Argonne National Laboratory. Rietveld refinements of synchrotron data were carried out using Fullprof Suite software to determine lattice parameters. Morphology and elemental composition of the obtained samples were determined using a scanning electron microscope (SEM) (JEOL JSM-7500F). Transmission electron microscope (TEM) - Energy Dispersive X-ray (EDS) mapping analyses were performed using a ThemIS operated at 300 kV at the National Center for Electron Microscopy of Lawrence Berkeley National Lab (LBNL). Thermogravimetric/differential thermal analysis (TG/DTA), Raman spectroscopy and Fourier transform infrared-attenuated total reflection (FTIR-ATR) analyses were performed at the Molecular Foundry of Lawrence Berkeley National Lab (LBNL). TG/DTA was

3

carried out in air on a TA Instruments Q5500 TGA-MS instrument using a heating rate of 5 $^\circ$C per minute. Raman spectra were collected with a Horiba Labram Aramis confocal Raman microscope with 532 nm laser. FTIR-ATR spectra were collected with a PerkinElmer Spectrum One instrument equipped with horizontal attenuated total reflection assembly (HATR) on a ZnSe 45-degree plate. *Ex-situ* soft X-ray absorption spectra (sXAS) were collected at beamline 10-1 of SSRL under ultrahigh vacuum (10^{-9} Torr) using the total electron yield (TEY) detector. All sXAS measurements were conducted with a 31-pole wiggler and a spherical grating monochromator with 20 mm entrance and exit slits, a 0.2 eV energy resolution and a 1 mm^2 beam spot.

Electrochemical Measurements

The composite electrodes were prepared by making a slurry of 70 wt.% sodium titanate, 20 wt.% acetylene black (Denka, 50% compressed), 5 wt.% carboxymethyl cellulose (CMC) and 5 wt.% Styrene-Butadiene Rubber (SBR) in water solution. The slurry was then cast onto carbon-coated aluminum foil. The electrodes were dried under vacuum at 100 $^\circ$C for 12 hours before being punched into 1/2-inch disks in diameter. The typical electrode loadings and thicknesses were ~ 1.0 - 1.5 mg cm^{-2} and 150 μm, respectively. 2032 type coin cells were assembled with metallic sodium foil (Sigma-Aldrich) as counter electrode, a GF/F glass fiber (Whatman) separator, and the chosen electrolyte. For most experiments, a solution of 0.5 M sodium tetraphenylborate (NaPhB$_4$, Sigma-Aldrich, as received) in diethylene glycol dimethyl ether (DEGDME, Anhydrous, Sigma-Aldrich, pre-dried with molecular sieve 3 Å) was used as electrolyte. Other electrolytic solutions were prepared in a similar manner (solvents were pre-dried with molecular sieve 3 Å, salts were used as received) and tested for the coulombic efficiency measurements, as listed in Figure 2. All the galvanostatic cycling measurements were performed using a VMP3 multichannel potentiostat/galvanostat (BioLogic) at a current rate of 8 mA g^{-1} (0.008 mA cm^{-2}) unless otherwise stated.

For the polyvinylidene fluoride (PVDF)-based composite electrodes, a slurry of 70 wt.% sodium titanate, 20 wt.% acetylene black (Denka, 50% compressed) and 10 wt.% PVDF in N-Methyl-2-pyrrolidone (NMP) solution was prepared and then cast onto carbon-coated aluminum foil. For the polytetrafluoroethylene (PTFE)-based electrode, an elastic dough was obtained by grinding 70 wt.% sodium titanate, 20 wt.% acetylene black (Denka, 50% compressed) and 10 wt.% PTFE, which was then tape-cast into a self-standing film. Binder-free electrodes were prepared by grinding 70 wt.% sodium titanate and 20 wt.% acetylene black (Denka, 50% compressed) powder mixtures together. The carbon-free composite electrodes were prepared by making a slurry of 90 wt.% sodium titanate, 5 wt.% CMC and 5 wt.% SBR in water solution. The slurry was then cast onto carbon-coated aluminum foil.

Results and discussion

The nonstoichiometric sodium titanate was synthesized *via* a two-step process. Cesium titanate Cs$_x$Ti$_{2-x/4}\square_{x/4}$O$_4$ was initially made using a classical solid-state reaction, and then ion-exchanged in aqueous sodium chloride solution to form the sodium-containing analog. For this work, the x = 0.74 phase was selected as an example to demonstrate its potential utility as anode material for sodium ion batteries.

4

Figures 1a & 1b show the XRD patterns of $Cs_{0.74}Ti_{1.815}\square_{0.185}O_4$ (termed CTO hereafter) before and after Cs^+/Na^+ ion exchange. Diffraction peaks of the as-prepared CTO (Figure 1a) can be indexed in the space group *Immm* (ICSD #202181[14]) with unit cell lattice parameters of a = 3.82570(2) Å, b = 17.30947(12) Å and c = 2.95881(2) Å (Table S1). The Rietveld refinement of the Na^+ ion-exchanged sample (termed NTO hereafter) in the *Immm* space group yielded a satisfactory fit with lattice parameters of a = 3.78058(1) Å, b = 17.90922(8) Å and c = 2.97811(1) Å (Figure 1b & Table S2), indicating that the body-centered orthorhombic symmetry was largely maintained upon Cs^+ extraction. Moreover, the interlayer distance (b/2) increased from 8.65 to 8.95 Å upon ion exchange despite the smaller Na^+ ion radius, suggesting hydration of interlayer Na^+ ions. The presence of interlayer water in NTO was confirmed by TG/DTA analysis (Figure 1c). The initial weight loss (ca. 3 %) below 100 ˚C is ascribed to physiosorbed water, while the major weight loss (ca. 9 %) upon further heating the sample to 500 ˚C is attributed to the removal of interlayer water. A nominal chemical formula of $Na_{0.74}Ti_{1.815}\square_{0.185}O_4 \bullet 1.27H_2O$ can be estimated for the Na^+ ion-exchanged sample. The presence of physiosorbed water was confirmed by FTIR-ATR spectroscopy. The IR spectrum of NTO showed a broad vibrational band centered at 3432 cm^{-1} along with a prominent peak at ca. 1634 cm^{-1}, which are typically assigned to the O−H stretching and bending modes of liquid water (Figure S1).[15, 16] The structural similarity of the as-synthesized CTO and its sodium containing form is evidenced by their similar Raman spectra, except for some spectral modifications induced by the different interactions between the interlayer cations and the octahedral TiO_6 layers (Figure S2). SEM/EDX analysis was further employed to assess the morphology and compositional changes that accompany the Cs^+/Na^+ ion exchange reaction. As seen in the SEM images, the platelet morphology of CTO powders was maintained during the ion exchange step (Figure S3). EDX analysis revealed an undetectable amount of Cs^+ ions after the ion exchange process (Figure 1d). Uniform elemental distribution of Na, Ti, and O at both the particle- and bulk- level were confirmed by EDX mapping (Figures 1e – 1h & S4).

5
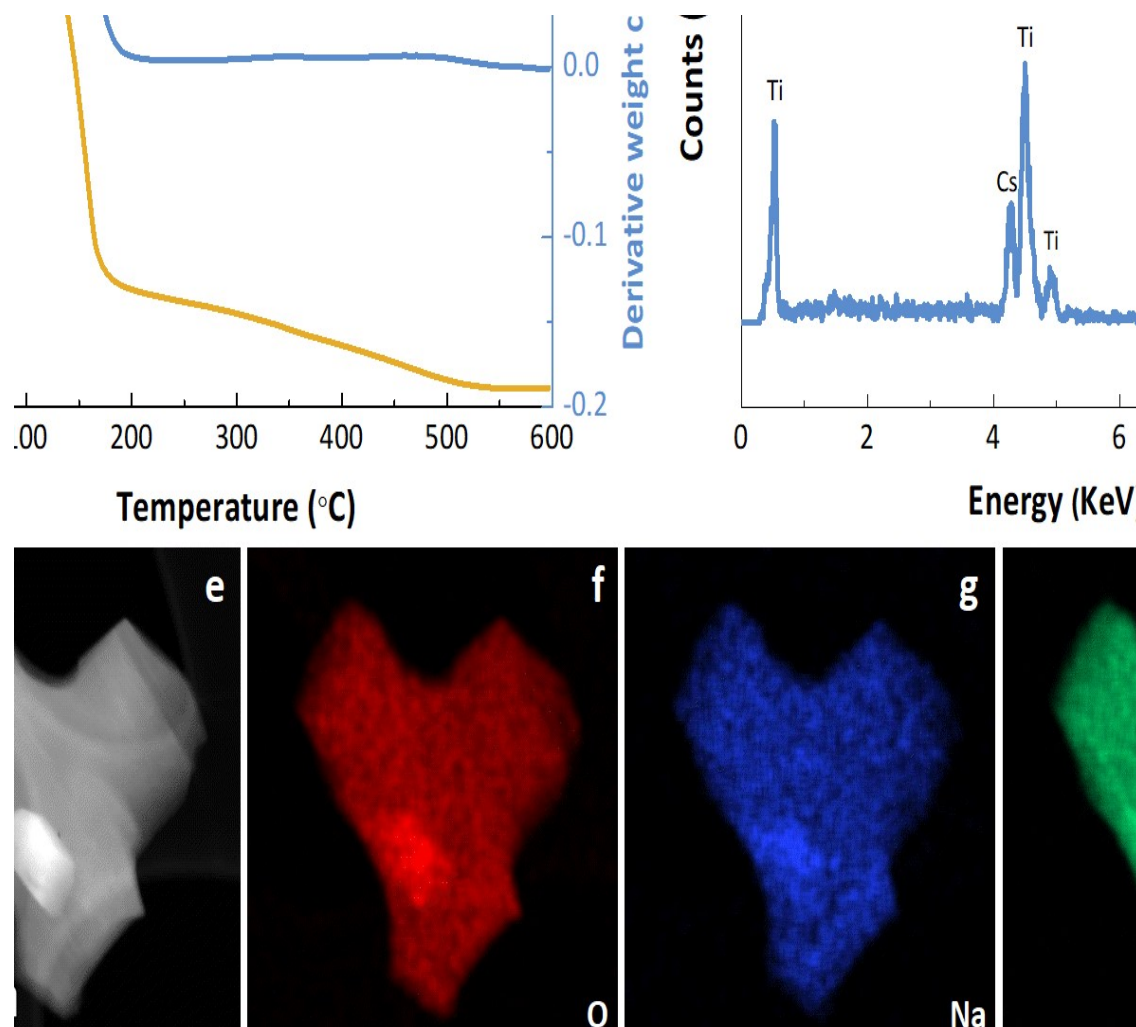
Figure 1 Rietveld refinement of the synchrotron XRD pattern of $Cs_{0.74}Ti_{1.815}\square_{0.185}O_4$ (CTO) (**a**) and the Na$^+$ ion exchanged sample (NTO) (**b**). Red line: observed; Black line: calculated; Blue line: difference; Green bar: Bragg position. **c.** TG/DTA curve of NTO. **d.** EDX spectra of CTO (blue line) and NTO (yellow line). TEM image (**e**) and element mapping images for O (**f**), Na (**g**) and Ti (**h**) of a single NTO particle.

The electrochemical properties of NTO were then evaluated in 2032-type coin cells with metallic sodium as counter/reference electrodes. Because of the low potentials at which sodium insertion takes place, low values of first-cycle Coulombic efficiencies (CE) (in the range of 30 % ~ 70 %), are commonly observed for titanium-based anode materials (Table 1).[17, 18] A low initial CE of the anode is detrimental to the energy density of full-cells where the Na$^+$ source is limited, because active ions are lost to side reactions and solid electrolyte interphase formation. The initial CE is known to be affected by the choice of electrolyte[4, 19, 20] and binder.[11, 21] Therefore, we decided to explore different electrolyte formulations, binders and electrode processing conditions, aiming to find an optimized electrode/electrolyte combination. The obtained CE in sodium half cells is compared in Figures 2 & S5. Among the systems investigated here, the 0.5 M NaPhB$_4$/DEGDME electrolyte exhibited the highest CE for both the initial (70.2 %) and the following cycles. From this point forward, 0.5 M NaPhB$_4$/DEGDME was used as our baseline electrolyte. For this part of

6

the study, NTO composite electrodes were exposed to ambient air for a short period of time (less than 10 min) during electrode punching. Previous work[14] has shown that lepidocrocite-type sodium titanates are very hygroscopic, with a tendency for water to insert into interlayer sites, due to their low charge densities. Indeed, simply avoiding the air-exposure by rigorously excluding air during processing improves the first-cycle CE from 70.2 % to 81 %, suggesting that water contributes to the first cycle inefficiency. Electrodes containing a mixture of CMC/SBR (1:1 in weight ratio) as binder deliver a higher initial CE than PVDF or PTFE (81.8 % as opposed to 51.2 % or 54.6 %). Notably, a high initial CE of 94.7 % is obtained for binder-free electrode consisting of NTO and carbon only. This result has two-fold implications: 1) ca. 13 % of first-cycle inefficiency is related to the decomposition of binder rather than to the irreversible sodiation of NTO and 2) CMC/SBR binder participates in the formation of the solid-electrolyte-interface (SEI), as previously shown using X-ray photoelectron spectroscopy for a lithium system.[22] Cells made with carbon-free electrodes (containing only NTO and CMC/SBR binder) show lower CE than the electrodes containing 20 wt.% carbon (71.2 % as opposed to 81.8 %) (Figure S6) because carbon improves the electrode electronic conductivity and favors the sodium deintercalation process. Overall, these results show that, with an appropriate electrolyte/binder combination, NTO gives comparable initial CE to hard carbon anodes[19], and provides a good electrolyte/electrode recipe to further evaluate the electrochemistry of NTO.

Figures 3a & 3b show the typical first- and second- cycle voltage profiles of CMC/SBR-based NTO electrodes cycled in the voltage range of 0.1 – 2.0 V *vs.* Na$^+$/Na at a current rate of 8 mA g^{-1} (0.008 mA cm^{-2}) in 0.5 M NaPhB$_4$/DEGDME electrolyte, where air has been rigorously excluded during processing of the electrodes. A discharge capacity of ca. 229 mAh g^{-1} is obtained during the second discharge. This is much higher than the 150 mAh g^{-1} measured under similar conditions (at a current rate of 8 mA g^{-1}) for another lepidocrocite-type sodium titanate having tetravalent titanium partially substituted by monovalent lithium (Na$_{0.8}$Ti$_{1.73}$Li$_{0.27}$O$_4$, termed NTLO in Figure 3b). NTLO and NTO have similar initial sodium contents (0.8 for NTLO, 0.74 for NTO), although somewhat different arrangements of species in the interlayer spaces. The gravimetric capacities of lepidocrocite titanates are generally limited by the number of available sites for ion intercalation rather than the amount of reducible Ti ions.[12] The theoretical capacity of NTO is 201 mAh g^{-1} if considering only the number of interlayer sites, less than the obtained capacity of 229 mAh g^{-1}. However, an augmented capacity of 230 mAh g^{-1} can be expected from NTO if the titanium vacancies are also considered. This suggests that vacancies in the titanium oxide layers may provide additional sites for sodium intercalation in NTO. A reversible capacity of ca. 213 mAh g^{-1} was obtained at current rate of 20 mA g^{-1} (0.021 mA cm^{-2}), a value comparable to anatase TiO$_2$ (Table 1) but at a lower average potential (~ 0.6 V *vs.* Na$^+$/Na for NTO and 0.8 V for *vs.* Na$^+$/Na for anatase TiO$_2$). Rate capability results obtained with current densities range from 20 to 6000 mA g^{-1} (0.021 to 6.239 mA cm^{-2}) are presented in Figure 3c. Reversible capacities of 197, 146 and 79 mAh g^{-1} were obtained at 50, 500 and 4000 mA g^{-1} (0.052, 0.52 and 4.161 mA cm^{-2}). This is better than carbon coated TiO$_2$ (40 nm)[7] and somewhat worse than carbon coated TiO$_2$ (11 nm)[7] and nano-TiO$_2$ (< 25 nm).[20] Note, however, that the NTO used here has a much larger particle size (hundreds of nm, Figures S3 & S4) than these examples. It is reasonable

7

to expect further performance improvement through materials engineering as previously elaborated (e.g., morphology control, surface modification, nanosizing et.).[7, 19, 20]

Figure 3d illustrates the discharge/charge capacity retention and CE over 50 cycles at the lowest current rate of 8 mA g^{-1} (0.008 mA cm^{-2}). A capacity of 151 mAh g^{-1} was obtained at the 50th cycle, corresponding to 66 % of the 2nd discharge capacity. Cells containing air-exposed NTO electrodes show improved capacity retention (75 % of the 2nd discharge capacity at the 50th cycle, Figure S7a).

Three plateau-like features are observed in the discharge/charge curves (Figure 3b), corresponding to the three consecutive pairs of reduction and oxidation peaks in the dQ/dV plot, (2nd cycle, Figure 3e). The two most prominent features are located at about 1.25 and 0.5 V, and a weaker one is observed near 0.65 V. The peaks at around 0.5 V are attributed to the Na$^+$ storage into interlayer space accompanied by Ti^{4+}/Ti^{3+} redox. The small peak separation (ca. 35 mV) of the peaks near 1.25 V indicates possible surface-controlled capacitive-like (absorption) contributions and are ascribed to Na$^+$ storage into surface-active sites. Based on the features of the dQ/dV plot, the whole discharge was deconvoluted into two regions (0.1 – 1.0 and 1.0 – 2.0 V $vs.$ Na$^+$/Na) and the capacity retention in each region was tracked. The capacity fades more rapidly in the high-voltage regime (1.0 – 2.0 V $vs.$ Na$^+$/Na) than in the low-voltage region (0.1 – 1.0 V $vs.$ Na$^+$/Na) (Figure 3f), suggesting that Na$^+$ storage into interlayer spaces is a more reversible process than Na$^+$ storage in surface-active sites for this electrode. Since the material shows less capacity fading between 0.1 – 1.0 V, improved cycling stability and lower capacity can be expected by decreasing the charge cut off voltage from 2.0 to 1.0 V. The achievable capacity between 0.1 – 1.0 V in the first charge is ca. 155.2 mAh/g.

To further assess the Na$^+$ storage processes in these two distinct voltage regions, cyclic voltammograms (CV) were recorded at various scan rates from 0.02 to 1.0 mV s^{-1} (Figure 4c). The peak current i in the CV experiment is related to the scan rate v by the power-law:

$$i = av^b \qquad (1)$$

where the b value is an indication of surface-controlled capacitive ($b = 1$) or diffusion-controlled intercalation ($b = 0.5$) reactions. b values of 0.78 and 0.67 were determined respectively for the peaks at 1.25 V $vs.$ Na$^+$/Na (R1 in Figures 4c & S8a) and at 0.5 V $vs.$ Na$^+$/Na (R2 in Figures 4c & S8a), suggesting hybrid processes involving both surface- and diffusion-controlled reactions. Further quantifying the current contribution ratios at each scan rate reveal a more surface-controlled capacitive contribution for the high-voltage process (R1, Figure 4e) than the low-voltage reduction step (R2, Figure S8b), e.g., 37.9 % for R1 and 22.5% for R2.

As previously mentioned, exposing the NTO electrode to air even briefly reduces the initial CE. It also modifies the discharge/charge voltage profile somewhat (Figures 4a & 4b). Correspondingly, the three pairs of peaks observed in the dQ/dV plot become broader and lower in intensity (Figure S9). Applying the same CV and power-law analyses to the air-exposed electrode (Figures 4d & S10a) reveals increased b-values (0.91 for the 1.25 V peak and 0.69 for the one at 0.5 V), which is indicative of increased current contributions from surface-controlled absorption reactions. Notably, for the reduction peak at ca. 1.25 V $vs.$ Na$^+$/Na, at a scan rate of 0.1 mV s^{-1}, 89 % of the contribution is capacitive-like for the air-exposed electrode, in contrast to 37.9

8

% for the air-free electrode (Figures 4e & 4f). The NTO phase is hygroscopic and, in most likelihood, surface functional groups provide extra redox active sites[23]. We speculate that air-exposure induces changes of surface properties, e.g., the formation of hydroxyl groups, which modify the nature of Na^+ storage reactions in surface-active sites (primarily in the high-voltage region) from diffusion-controlled intercalation to more reversible surface-controlled absorption. This is consistent with the observation that capacity fading in the high-voltage (Na^+ storage into surface-active sites, 1.0 – 2.0 V *vs.* Na^+/Na) region for the air-exposed electrode (35.6 % of the 2nd cycle capacity at the 30th cycle) is less severe than for the electrode that was not exposed (29.6 % of the 2nd cycle at 30th cycle) (Figure S7b). The formation of hydroxyl groups agrees with sXAS results showing that the Ti L_3 edge position shifts slightly to lower energy after air-exposure (Figure S11). Although our hypothesis sounds reasonable, it should be noted that density functional theory (DFT) calculations suggest limited effects in enhancing Na^+ absorption at carbon surfaces for hydroxyl groups.[24] Nevertheless, our results highlight the sensitivity of the electrochemistry of these materials to air (moisture) exposure.
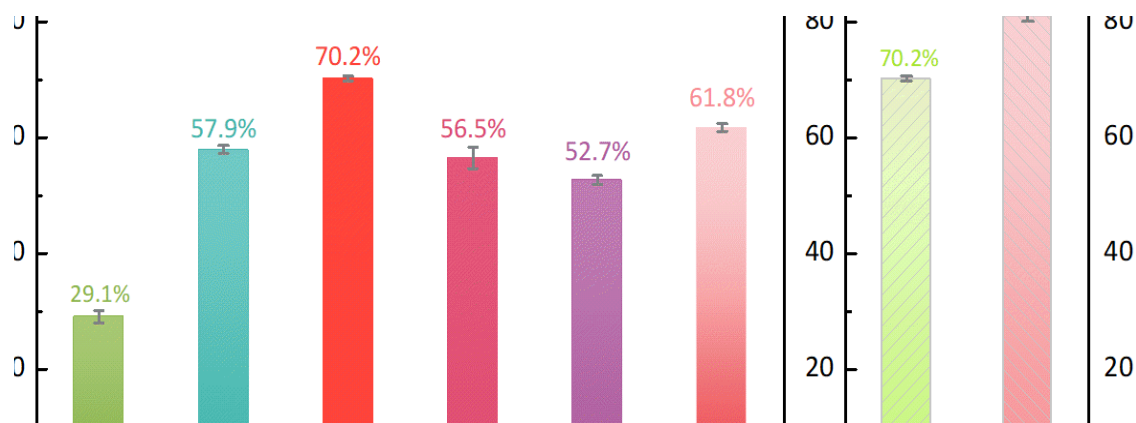
Figure 2 Average first-cycle CE of sodium half-cells cycled with various electrolyte formulations (**a**), NTO composite electrodes with/without short-term (less than 10 min) air-exposure (**b**), and NTO composite electrodes containing different binders (**c**). All the cells were cycled at current rate of 8 mA g^{-1} (0.008 mA cm^{-2}) between 0.1 and 2.0 V *vs.* Na^+/Na. The error bars represent the standard deviation of the average values of CE.

9

Table 1 Sodium storage properties and half-cell test conditions of titanium-based anode materials reported for sodium-ion batteries. Parameters for hard carbon are included for the sake of comparison.

ANODE MATERIAL	ELECTROLYTE	BINDER	E (V)	CURRENT (MA G^{-1})	1ST CE	REV. CAP. (MAH G^{-1})	REF.
$Na_2Ti_3O_7$	1M $NaClO_4$ EC/PC (1:1 v/v)	Kynar	0.3	0.1C	41.6%	205	[10]
Anatase TiO_2 *C-coated*	1M $NaClO_4$ EC/PC (1:1 v/v)	PVDF	0.8	33.5	30.6% *38.2%*	175 *227*	[7]
C-coated $Na_2Ti_6O_{13}$	1M $NaClO_4$ EC/DEC (1:1 v/v)/5% FEC	PVDF	0.85	50	52.6%	105	[25]
Anatase TiO_2	1M $NaPF_6$ DEGDME 1M $NaPF_6$ EC/DEC	PVDF	0.8	50	56% 40%	217 181	[20]
$NaTi_3O_6(OH)\cdot 2H_2O$ (dehydrated)	1M $NaPF_6$ EC/DMC (3:7 *n/n*)	CMC	0.3	20	65%	200	[9]
$Na_{0.8}Ti_{1.73}Li_{0.27}O_4$	1M $NaPF_6$ EC/DMC (3:7 *n/n*)	PVDF *PAA*	0.5	0.2 mA cm^{-2}	31.2% 48%	105 *140*	[11]
Blue TiO_2(B) W-TiO_2(B)	1M $NaClO_4$ PC/5% FEC	CMC	0.8	83.75	41.5% 37%	200 160	[26]
$Li_4Ti_5O_{12}$	1M NaFSI EC/DEC (4:6 v/v)	CMC PVDF NaAlg	0.91	17.5	81% 76% 75.1%	155 Very poor 148	[21]
$Na_2Ti_9O_{19}$	1M $NaPF_6$ EC/DMC (1:1)	CMC	ca. 0.6	20	57%	160	[27]
$NaTiO_2$	1M $NaPF_6$ EC/DEC (1:1 v/v)	PTFE	1.0	0.1C	82%	152	[28]
$Na_{0.66}Ti_{0.22}Li_{0.78}O_2$	1M $NaClO_4$ EC/DEC (4:6 v/v)	PVDF	0.75	10.6	74%	100	[29]
Hard carbon	0.5M $NaBPh_4$ DME 0.5M $NaPF_6$ DME	CMC	0–0.1	20	95% 94.5%	260.8 261.0	[19]

	1M NaPF$_6$ EC/DEC				92.5%	250.5	
Na$_{0.74}$Ti$_{1.815}$□$_{0.185}$O$_4$· 1.27H$_2$O	0.5M NaBPh$_4$ DEGDME	CMC/ SBR	0.6	20	81.8 %	213	This work
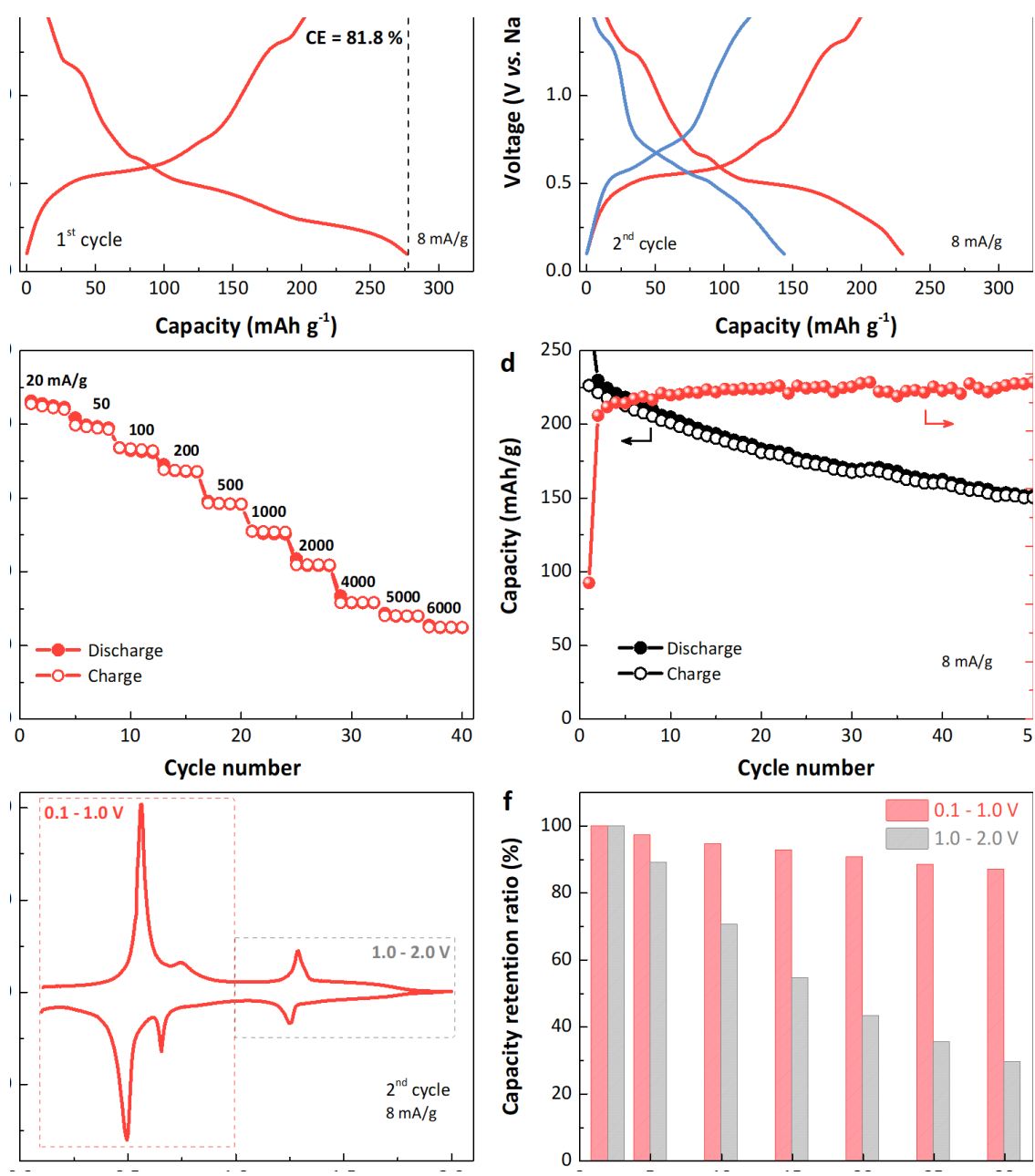
Figure 3 Typical first- (**a**) and second- cycle (**b**, red curve) voltage profiles of NTO half-cells. Air was rigorously excluded during electrode processing for these experiments. The second-cycle voltage profile of Na$_{0.8}$Ti$_{1.73}$Li$_{0.27}$O$_4$ (NTLO) measured at current rate of 8 mA g^{-1} is also included for comparison (**b**, blue curve). (**c**) Discharge/charge capacities of NTO half-cells cycled at current rates from 20 to 6000 mA g^{-1} (0.021 to 6.239 mA cm^{-2}). (**d**) Discharge/charge capacity retention of NTO half-cells over 50 cycles. The corresponding Coulombic efficiency is plotted on the secondary *y*-axis. (**e**) Second cycle *d*Q/*d*V plot of

NTO. (**f**) Capacity retention in the voltage regions of 0.1 - 1.0 V (red column) and 1.0 - 2.0 V (grey column) *vs.* Na⁺/Na. The absolute capacities were normalized to the 2ⁿᵈ cycle to obtain the capacity retention ratio (%). All the cells were cycled at a current rate of 8 mA g⁻¹ (0.008 mA cm⁻²) between 0.1 and 2.0 V *vs.* Na⁺/ Na, except for the rate test. A solution of 0.5 M NaPhB₄ in DEGDME was used as electrolyte.
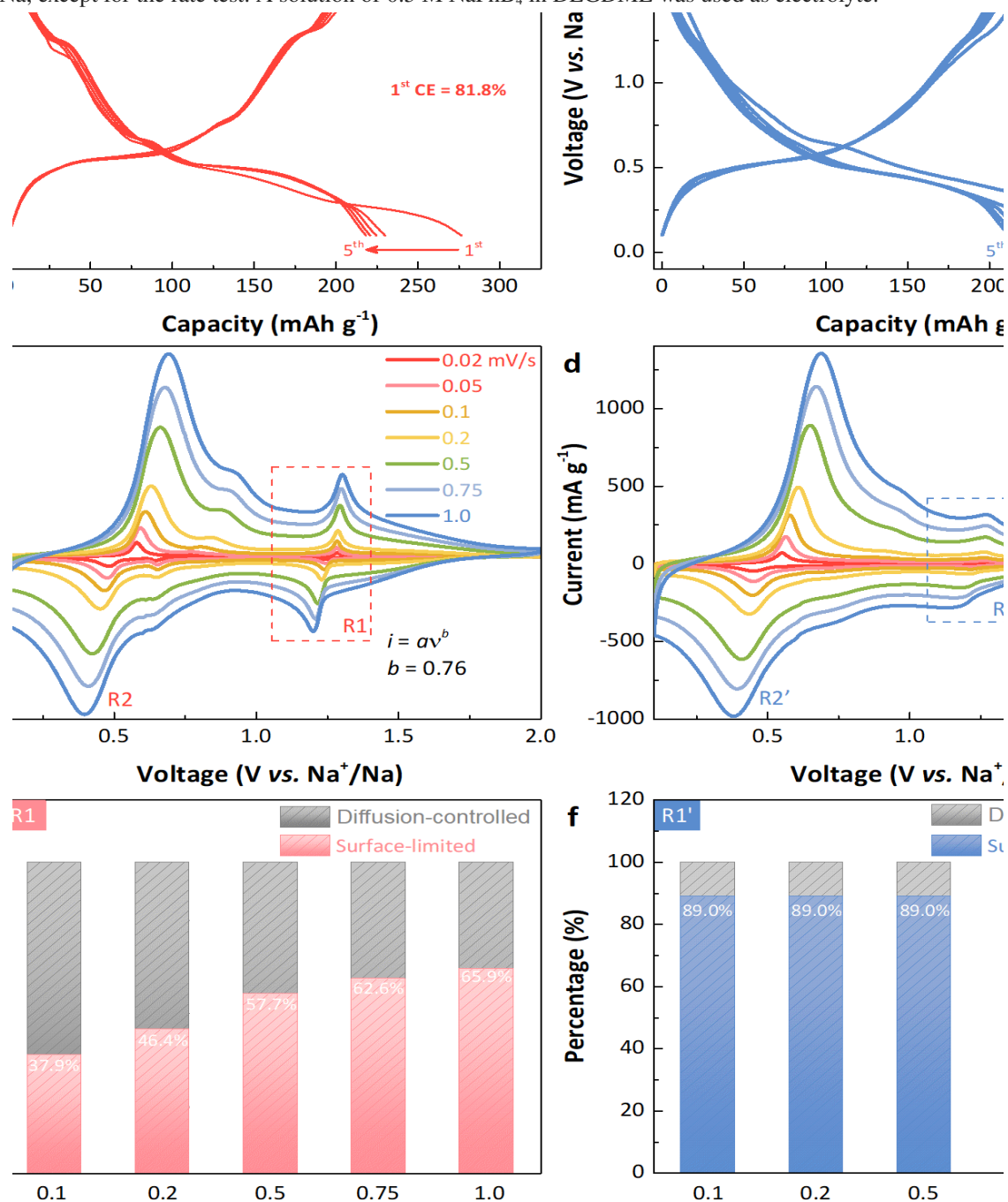
Figure 4 Initial five cycles of sodium half-cells containing NTO composite electrodes without (**a**, 'air-free electrode') and with (**b**, 'air-exposed electrode') 10 min ambient air-exposure. Cyclic voltammograms of air-free (**c**) and air-exposed (**d**) NTO electrodes measured at scan rates from 0.02 to 1.0 mV s⁻¹. The normalized contribution ratio of diffusion- (intercalation) and surface- controlled(absorption) reactions for

the reduction peaks at ca. 1.2 V *vs.* Na$^+$/Na: "R1" for air-free (**e**) and "R1''" for air-exposed (**f**) NTO electrodes.

Conclusions

A nonstoichiometric lepidocrocite-type sodium titanate derived from a cesium titanate $Cs_xTi_{2-x/4}\square_{x/4}O_4$ ($x = 0.74$) precursor shows promise as an anode material for sodium ion batteries. It can deliver over 200 mAh g^{-1} at moderate rates at a low average potential of about 0.6 V *vs.* Na$^+$/ Na with good reversibility. By careful electrode engineering and appropriate selection of electrolytic solution, first cycle coulombic efficiencies could be improved to nearly 95%. An analysis of the electrochemical behavior shows that the capacity can be attributed to Na$^+$ storage into interlayer spaces, surface-active sites and possibly titanium vacancies through hybrid intercalation and adsorption reactions. Exposing the electrode to air slightly decreases the first cycle columbic efficiencies and changes the voltage profile. Somewhat surprisingly, however, better reversibility is obtained for air-exposed electrodes, most likely due to an increase in more reversible Na$^+$ adsorption into surface-active sites.

Conflict of interest

The authors declare no conflict of interests.

Data availability

The data that support the findings of this study are available in the electronic supplementary materials.

References

1. J.-M. Tarascon, Joule **4** (8), 1616-1620 (2020).
2. I. Hasa, S. Mariyappan, D. Saurel, P. Adelhelm, A. Y. Koposov, C. Masquelier, L. Croguennec and M. Casas-Cabanas, Journal of Power Sources **482** (2021).
3. S. Mariyappan, Q. Wang and J. M. Tarascon, Journal of The Electrochemical Society **165** (16), A3714-A3722 (2018).
4. B. Zhang, G. Rousse, D. Foix, R. Dugas, D. A. Corte and J. M. Tarascon, Adv Mater **28** (44), 9824-9830 (2016).
5. M. Shirpour, J. Cabana and M. Doeff, Energy & Environmental Science **6** (8) (2013).
6. S. Guo, J. Yi, Y. Sun and H. Zhou, Energy & Environmental Science **9** (10), 2978-3006 (2016).
7. M. N. Tahir, B. Oschmann, D. Buchholz, X. Dou, I. Lieberwirth, M. Panthofer, W. Tremel, R. Zentel and S. Passerini, Adv Energy Mater **6** (4), 1501489 (2016).
8. M. M. Doeff, J. Cabana and M. Shirpour, Journal of Inorganic and Organometallic Polymers and Materials **24** (1), 5-14 (2013).
9. J. Alvarado, G. Barim, C. D. Quilty, E. Yi, K. J. Takeuchi, E. S. Takeuchi, A. C. Marschilok and M. M. Doeff, Journal of Materials Chemistry A **8** (38), 19917-19926 (2020).
10. A. Rudola, K. Saravanan, C. W. Mason and P. Balaya, Journal of Materials Chemistry A **1** (7) (2013).
11. M. Shirpour, J. Cabana and M. Doeff, Chemistry of Materials **26** (8), 2502-2512 (2014).
12. I. M. Markus, S. Engelke, M. Shirpour, M. Asta and M. Doeff, Chemistry of Materials **28** (12), 4284-4291 (2016).
13. A. Katogi, K. Kubota, K. Chihara, K. Miyamoto, T. Hasegawa and S. Komaba, ACS Applied Energy Materials **1** (8), 3630-3635 (2018).
14. T. Sasaki, Y. Komatsu and Y. Fujiki, J. Chem. Soc., Chem. Commun., 817-818 (1991).
15. J. E. Bertie and Z. Lan, Applied Spectroscopy **50** (8), 1047-1057 (1996).
16. A. A. Kananenka and J. L. Skinner, J Chem Phys **148** (24), 244107 (2018).
17. H. Hou, X. Qiu, W. Wei, Y. Zhang and X. Ji, Advanced Energy Materials **7** (24) (2017).
18. H. He, D. Sun, Y. Tang, H. Wang and M. Shao, Energy Storage Materials **23**, 233-251 (2019).
19. Y. Morikawa, Y. Yamada, K. Doi, S.-i. Nishimura and A. Yamada, Electrochemistry **88** (3), 151-156 (2020).
20. Z.-L. Xu, K. Lim, K.-Y. Park, G. Yoon, W. M. Seong and K. Kang, Advanced Functional Materials **28** (29) (2018).
21. Y. Sun, L. Zhao, H. Pan, X. Lu, L. Gu, Y. S. Hu, H. Li, M. Armand, Y. Ikuhara, L. Chen and X. Huang, Nat Commun **4**, 1870 (2013).
22. L. El Ouatani, R. Dedryvère, J. B. Ledeuil, C. Siret, P. Biensan, J. Desbrières and D. Gonbeau, Journal

of Power Sources **189** (1), 72-80 (2009).

23. Y. Shao, J. Xiao, W. Wang, M. Engelhard, X. Chen, Z. Nie, M. Gu, L. V. Saraf, G. Exarhos, J. G. Zhang and J. Liu, Nano Lett **13** (8), 3909-3914 (2013).

24. F. Sun, H. Wang, Z. Qu, K. Wang, L. Wang, J. Gao, J. Gao, S. Liu and Y. Lu, Advanced Energy Materials (2020).

25. J. Wang, J. Bi, W. Wang, Z. Xing, Y. Bai, M. Leng and X. Gao, Journal of The Electrochemical Society **167** (9) (2020).

26. Y. Zhang, Z. Ding, C. W. Foster, C. E. Banks, X. Qiu and X. Ji, Advanced Functional Materials **27** (27) (2017).

27. S. S. M. Bhat, B. Babu, M. Feygenson, J. C. Neuefeind and M. M. Shaijumon, ACS Appl Mater Interfaces **10** (1), 437-447 (2018).

28. D. Wu, X. Li, B. Xu, N. Twu, L. Liu and G. Ceder, Energy & Environmental Science **8** (1), 195-202 (2015).

29. Y. Wang, X. Yu, S. Xu, J. Bai, R. Xiao, Y. S. Hu, H. Li, X. Q. Yang, L. Chen and X. Huang, Nat Commun **4**, 2365 (2013).

15